

High-Efficiency Resonant Beam Charging and Communication

Yunfeng Bai, Qingwen Liu, *Senior Member, IEEE*, Xin Wang, *Fellow, IEEE*,
Yudan Gou, Bin Zhou and Zhiyong Bu

Abstract—With the development of Internet of Things (IoT), demands of power and data for IoT devices increase drastically. In order to resolve the supply-demand contradiction, simultaneous wireless information and power transfer (SWIPT) has been envisioned as an enabling technology by providing high-power energy transfer and high-rate data delivering concurrently. In this paper, we introduce a high-efficiency resonant beam (RB) charging and communication scheme. The scheme utilizes the semiconductor materials as gain medium, which has a better energy absorption capacity compared with the traditional solid-state one. Moreover, the telescope internal modulator (TIM) are adopted in the scheme which can concentrate beams to match the gain size, reducing the transmission loss. To evaluate the scheme SWIPT performance, we establish an analytical model and study the influence factors of its beam transmission, energy conversion, output power, and spectral efficiency. Numerical results shows that the proposed RB system can realize 16 W electric power output with 11 % end-to-end conversion efficiency, and support 18 bit/s/Hz spectral efficiency for communication.

Index Terms—Optical communication; Resonant beam communications; Wireless power transfer; Wireless charging

I. INTRODUCTION

Accompany by the growth of the Internet of Things (IoT), network capacity continues to increase due to rapidly growing number of devices [1]. At the same time, the energy consumption of mobile devices is also increasing dramatically to support high-performance communication and computation [2]. Facing these challenges, various technologies have been promoted, e.g., wireless power transfer (WPT), ultra-dense cloud radio access networks, etc. [3], [4]. Among them, WPT for providing unlimited energy supply is undoubtedly one of the most attractive solutions [5]. Compared with wired power supply, WPT is flexible and suitable for mobile devices; compared with battery, WPT is not restricted by battery's capacity, weight, or volume [6], [7].

Based on the WPT, simultaneous wireless information and power transfer (SWIPT) technology has attracted great attention by researchers to address both the energy and data

Y. Bai, and Q. Liu, are with the College of Electronics and Information Engineering, Tongji University, Shanghai, China, (email: baiyf@tongji.edu.cn, qliu@tongji.edu.cn).

Xin Wang is with the Key Laboratory for Information Science of Electromagnetic Waves, Department of Communication Science and Engineering, Fudan University, Shanghai 200433, China (e-mail: xwang11@fudan.edu.cn).

Yudan Gou is with the College of Electronics and Information Engineering, Sichuan University, Chengdu 610065, China(gouyudan@scu.edu.cn).

B. Zhou, and Z. Bu, are with the Key Laboratory of Wireless Sensor Network and Communications, Shanghai Institute of Microsystem and Information Technology, Chinese Academy of Sciences, Shanghai, China, (email: bin.zhou@mail.sim.ac.cn, zhiyong.bu@mail.sim.ac.cn).

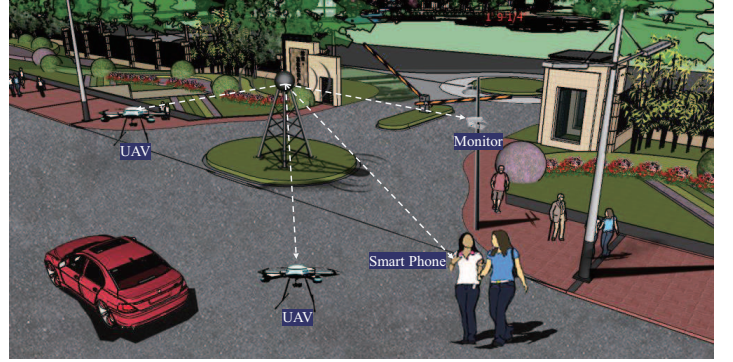


Fig. 1. Application scenarios of SWIPT (UAV: unmanned aerial vehicle)

demands at the same time (Fig. 1). SWIPT technologies have many forms with different system structure depending on the carrier. SWIPT system utilizing radio frequency (RF) as carrier is one of typical schemes. It depends on the mature RF communication technology, which has the characteristics of low cost, long transfer distance, and expansive coverage. However, humans may be physical damage in the presence of high density RF radiation. Thus, the researchers must gain more thorough understanding of potential health and safety impacts associated with the usage of SWIPT in public settings [8]. Optical beams such as visible light can also be applied as the SWIPT carrier. The optical SWIPT scheme effectively harnesses the unique properties of light to support high-power energy transfer. This approach also offers significant communication advantages, including access to an extensive license-free spectrum, zero electromagnetic interference, and the capability for high-speed data transmission [9], [10]. However, typical optical beams schemes are limited by alignment, safety, etc.

As one of the optical beams scheme, resonant beam system (RBS) was proposed for self-alignment, and radiation safety light transmission [11], [12]. The transmitter of the RBS is combined with the receiver to form a spatially separated resonator (SSR). The resonant beam generates in the cavity and carrying energy and information transfers between the transmitter and the receiver through the reflectors. Due to the beam concentration characteristics, RBS can support high power transfer [13]. Moreover, by cooperating retro-reflectors, RBS enables self-alignment between the transmitter and the receiver for mobile SWIPT [14]. When the light path between the transmitter and the receiver is blocked thanks to the

separate resonant cavity structure, the cyclic reciprocating process of the resonant beam in the cavity will interrupt immediately, which prevents foreign objects from continuous radiative exposure, ensuring the human safety [15]. Besides, as the aforementioned statement, since the light beam is the signal carrier in the RBS, it can allow high-rate data transfer [16]. Due to these remarkable advantages, the RBS has been applied in various SWIPT applications such as unmanned aerial vehicles (UAV), smartphones, monitors, etc. [17], [18].

The theoretical model, system design, deployment of the RBS have been studied in the literature recently. Firstly, Zhang *et al.* verified that the RBS can support 2 W WPT with 1 % end-to-end conversion efficiency in experiment [13]. Sheng *et al.* demonstrated an efficient, long-distance scheme using cat-eye reflectors to realize transmitter alignment, a telescope to concentrate beams, and adopting aspheric lenses to fix spherical aberration [19]. In [20], Zhang *et al.* characterized a long vertical external-cavity surface-emitting lasers resonator scheme for wireless charging. Moreover, to support multi-devices access into the RBS, Xiong *et al.* proposed a time-division multiple access (TDMA) RBS design for wireless power transfer [21]. Xiong *et al.* proposed the RB communication design and the analytical model in [22]. Liu *et al.* presented the basic SWIPT model of the RBS and demonstrated its mobile ability using the retro-reflectors [14]. To evaluate the safety of the RBS, Fang *et al.* proposed an analytical model based on electromagnetic field analysis and assessed its safety with external object invasion [15].

Previous research has underscored the features and potential of Resonant Beam (RB) technology in Simultaneous Wireless Information and Power Transfer. Nevertheless, the original RB scheme still has been challenged by significant energy conversion losses, resulting in a merely approximate 1% energy conversion efficiency across short distances [13]. The relatively low conversion efficiency of this technology presents challenges for its application in power supply scenarios for devices under a low-carbon and energy-saving context. Moreover, due to the suboptimal transmission efficiency, the system requires a greater input to satisfy the power demand at the output end. This situation imposes further challenges on system cooling, safety, and component durability.

In this study, we present a novel RB-SWIPT scheme designed to elevate both power transmission efficiency and communication efficacy. We propose the use of a semiconductor gain medium, in contrast to the conventional solid-state medium. Semiconductors exhibit superior energy absorption capacity from the pump source, thus promoting a more effective energy level transition and population inversion efficiency. Consequently, the power threshold decreases, thereby improving the overall conversion efficiency.

Additionally, we integrate a telescope internal modulator (TIM) into the resonator. The TIM serves to compress the beam, thereby harmonizing with the smaller dimensions of the gain medium and subsequently reducing transmission loss. This strategic modification underlines our commitment to enhancing the efficiency of SWIPT systems.

The contributions of this paper are summarized as follows:

- A high-efficiency RB-SWIPT scheme is proposed. By

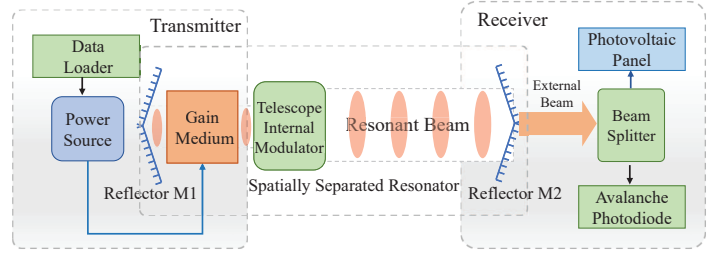


Fig. 2. High-efficiency resonant beam SWIPT system

adopting the semiconductor gain medium and the telescope internal module, the scheme can achieve long-range, high-rate, and energy conversion efficiency enhanced SWIPT.

- An analytical model of the proposed scheme is developed, which can describe the energy conversion, the beam propagation, the electric power output, and data transfer capability of the system. An evaluation for system performance and a guidance for parameters optimization is provided.

The remainder of this paper is structured as follows: Section II details the high-efficiency RBS model, including descriptions of the semiconductor gain medium and TIM. Section III presents a numerical evaluation of the system's performance. Concerns related to the beam splitting process are discussed in Section IV. Finally, Section V concludes the paper.

II. SCHEME ANALYSIS AND MODEL ESTABLISHMENT

In this section, we will state the function principle of the scheme on realizing high-efficiency resonant beam charging and communication and develop the analytical model.

A. System Structure and Semiconductor Gain

The system structure of the proposed RB-SWIPT scheme is briefly depicted in Fig. 2. Overall, the system can be divided into three parts: transmitter, receiver, and spatially separated resonator. The transmitter is mainly composed of a gain medium, a pump source and a data loader. The data loader can load the electric signal into the pump source for data transfer. Then, the pump source releases beam carrying the data signal in the form of optical radiation to the gain medium. The gain medium receives the energy and occurs the stimulated absorption, spontaneous emission, and stimulated emission, generating photons to form resonant beams. The receiver mainly includes three elements: photovoltaic (PV) panel module, beam splitter, and avalanche photodiode (APD) module [23], [24]. The beam splitter is applied to accept the external beams output from the M2 and split them into two rays. for independent energy harvesting and data receiving. The PV module receives one of the rays for energy harvesting where the optical energy can be converted into electrical power after photoelectric conversion. The APD module captures the remaining rays for data reception, where the light signal is detected. The spatially separated resonator is made by reflectors M1, M2, and a TIM. Among them, M1 and M2

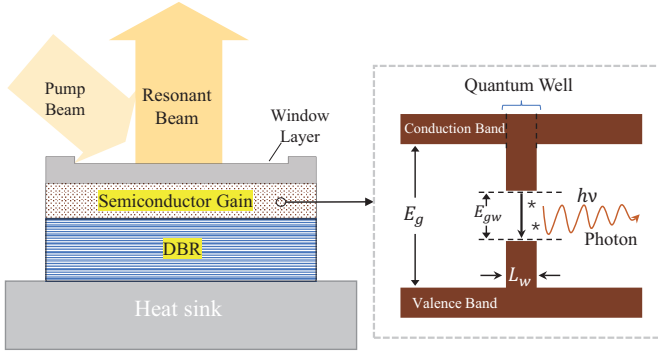


Fig. 3. Transmitter structure and operating principles of the semiconductor gain (DBR: distributed Bragg reflector; E_g , E_{gw} : energy level difference; L_w : quantum well length; $h\nu$: photon energy)

constitute the resonant cavity for beams oscillation. The TIM is placed on the optical path in front of the gain, which is used to change the phase of the resonant beam for beam compression and promoting the beam incidence.

The proposed RB scheme applies the semiconductor materials to compose the gain medium for efficiency enhanced. Semiconductor material utilizes the recombination of electrons in the conduction band and holes in the valence band to generate simulated radiation [25], which has the following characteristics: 1) The materials with different ingredients on gain medium developing window layer, active area, and distributed Bragg reflector layer (DBR) have a band-gap difference forming a potential barrier. It will confine electrons and holes within the gain area, which is conducive to the recombination of electrons and holes; 2) The active area and the cladding layers have a refractive index difference. When photons transfer on the material boundary, they will be reflected back to the active area. As a result, the light field can be restricted in the active area, which causes more stimulated radiation generation; 3) The semiconductor gain can be made as a hetero-junction quantum well structure. This structure (Fig. 3) can further reduce the thickness of the active layer to the nano-level producing the quantum effect, which makes the limitation of carriers and light fields be further strengthened, and causes the energy level difference decreasing from E_g to E_{gw} [26], [27]. Thanks to these characteristics, the particle conversion loss in the semiconductor gain is significantly minimized, resulting in a substantial reduction of the threshold value.

B. Resonant Beam Power and Conversion Efficiency

In the gain medium of the proposed optical system, photons are generated and subsequently propagate within the cavity. This process results in the formation of a resonant beam. The resonant beam, functioning as a carrier, transmits both energy and signal to the designated receiver.

To assess the transmission efficacy of the system, the beam power output at reflector M2 serves as a crucial figure of merit. Additionally, the system exhibits a characteristic threshold power due to inherent energy losses. The output beam is only generated when the input power surpasses this threshold

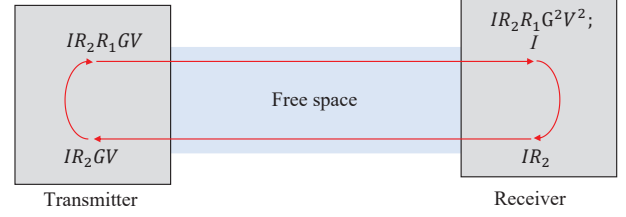


Fig. 4. End-to-end energy cycle (I : initial energy density; R_1, R_2 : reflectivity of M1, M2; G : gain factor; V : Path loss)

condition. Furthermore, the relationship between input and output power is governed by a conversion efficiency ratio. This ratio is a function of the energy conversion process occurring at each stage within the system. Based on the cyclic power principle and materials characteristic of the gain medium [28], [29], the external beam power can be defined as:

$$P_{\text{beam}} = (P_{\text{in}} - P_{\text{th}}) \eta_s, \quad (1)$$

where P_{in} denotes the input electric power, P_{th} expresses the threshold power, and η_s is the slope efficiency.

Firstly, η_s is related to the system structure such as the reflectivity of M1, which can be depicted as:

$$\eta_s = \frac{\eta_{pc} \eta_{pa} \lambda_{\text{pump}} \ln(R_2)}{\lambda_{\text{beam}} \ln(R_1 R_2 V)}, \quad (2)$$

where R_1 and R_2 denote the reflectivity of the reflectors M1 and M2, η_{pc} is the pump conversion efficiency, λ_{beam} , λ_{pump} represent the wavelength of resonant beams and pump beams, $V = V_c V_d$ expresses overall energy losses which mainly includes constant loss V_c (absorption dispersion of reflectors and air, internal loss in the gain) and beam diffraction loss V_d .

Secondly, P_{th} is determined by the gain medium, which can be expressed as:

$$P_{\text{th}} = \frac{A_s h c l N_{\text{th}}}{\lambda \eta_{pc} \eta_{pa} \tau}, \quad (3)$$

where A_s expresses the effective active cross-section, h denotes the Planck constant, c is the speed of light in vacuum, λ represents the beam wavelength, l is the length of the gain medium, N_{th} denotes the threshold carrier density in gain medium, η_{pa} expresses the pump absorption efficiency, and τ is the carrier attenuation time.

Normally, τ can be expressed as [29]:

$$\tau = (\alpha + \beta N_{\text{th}} + \gamma N_{\text{th}}^2)^{-1}, \quad (4)$$

where α , β and γ express recombination coefficients of the gain medium. N_{th} is related to the gain factor, which can be described as:

$$N_{\text{th}} = N_0 \exp(g/g_0), \quad (5)$$

where g_0 is gain coefficient under low pump power, N_0 denotes the transparency carrier density, and g expresses the saturation gain coefficient.

To define the parameter g , it is essential to analyze the energy saturation condition, characterized by an equilibrium between gain and loss within the system [28]. According to Fig. 2, the spatially separated resonator cavity includes

reflectors M1, M2, TIM, and gain medium. During the propagation of the resonant beam within the cavity, optical elements, notably M1, either absorb or reflect a portion of the beam, resulting in energy losses. Conversely, energy is gained in the gain medium. Consequently, if the beam, after completing one round-trip within the cavity, returns to its point of origin with its energy unaltered, it can be inferred that the system has attained a state of equilibrium between loss and gain. This specific equilibrium state is referred to as the saturation condition. From Fig. 4, after one-trip energy cycle, the initial energy density will become $IR_2R_1G^2V^2$ from I . When the saturation condition is satisfied, the $IR_2R_1G^2V^2$ should equal to I , and parameters have the relationship as:

$$R_1R_2G^2V^2 = 1, \quad (6)$$

where $G = \exp(\Gamma gl)$ expresses the overall gain factor (each time the beam travels through the gain, the beam energy intensity will increase by G times), R_1 and R_2 can be considered as the beam emission ratio of M1 and M2. At this time, g can be depicted as:

$$g = -\frac{\ln(R_1R_2V^2)}{2l}. \quad (7)$$

Further, taking the (7) into (5), the N_{th} can be denoted as:

$$N_{\text{th}} = N_0(R_1R_2V^2)^{-(2g_0l\Gamma)^{-1}}, \quad (8)$$

where Γ is the longitudinal confinement factor.

Finally, based on aforementioned formulas, the P_{beam} presented in (1) can be depicted. At the end, the beam transmission efficiency can be defined as:

$$\eta_b = \frac{\eta_{pc}\eta_{pa}\lambda_{\text{pump}}\ln(R_2)}{\lambda_{\text{beam}}\ln(R_1R_2V)} \left(1 - \frac{A_s h c l N_{\text{th}}}{\lambda \eta_{pc} \eta_{pa} \tau P_{\text{in}}}\right). \quad (9)$$

C. Beam Transmission Description and Diffraction Loss

To analyze the resonator structure, the process of beam transmission in the resonator should be described at first. In this paper, we adopt beam vectors and transmission matrices to define the beam propagation. Specifically, based on the beam physics characteristics (straight line propagating), we can depict it as $\vec{r} = (x, \theta_x)$, where x expresses the position parameter on the coordinate axis and θ_x represents the propagation direction of the beam. Assuming a beam originates at a specific point and propagates in free space from x_1 to x_2 , with an initial transmission angle denoted as θ_1 , the beam's trajectory can be represented using vector notation. Initially, the beam vector is expressed as $\vec{r}_1 = (x_1, \theta_1)$. As the beam progresses along its path to a position z , its vector representation evolves to $\vec{r}_2 = (x_2, \theta_2)$, indicating the change in both position and transmission angle. The process of vectors conversion from \vec{r}_1 to \vec{r}_2 can utilize matrix \mathbf{M} to express, which is $\vec{r}_2 = \mathbf{M}\vec{r}_1$. Moreover, when the beam passes through a series of optical components, the entire process can be expressed as the matrices of these components multiplied in the corresponding order.

By employing the aforementioned beam vectors and the transmission matrices, it is possible to define the optical elements and characterize the beam transfer within the cavity.

Firstly, we adopt it to depict the reflectors. The reflectors introduce in the scheme involving in a convex lens (focal length: f) and a reflective mirror. The reflective mirror is located at the exit pupil of the lens with distance d , and its surface is flat (infinite focal length). Using the typical matrices' expression of lenses and mirror [28], the reflector can be described as:

$$\begin{aligned} \mathbf{M}_r &= \begin{bmatrix} 1 & f \\ 0 & 1 \end{bmatrix} \begin{bmatrix} 1 & 0 \\ -1/f & 1 \end{bmatrix} \begin{bmatrix} 1 & d \\ 0 & 1 \end{bmatrix} \begin{bmatrix} 1 & 0 \\ 0 & 1 \end{bmatrix} \\ &= \begin{bmatrix} 1 & d \\ 0 & 1 \end{bmatrix} \begin{bmatrix} 1 & 0 \\ -1/f & 1 \end{bmatrix} \begin{bmatrix} 1 & f \\ 0 & 1 \end{bmatrix} \\ &= \begin{bmatrix} -1 & 0 \\ 1/f_r & -1 \end{bmatrix}, \end{aligned} \quad (10)$$

where

$$f_r = \frac{f^2}{2(d-f)}. \quad (11)$$

Reflectors can reflect incident beams back toward the parallel path of the original one, which is precondition of the self-alignment [14]. To realize ideal retro-reflect in the proposed reflectors, we design $d = f$, which denotes the mirror is put at the focal point of the lens.

To effectively compress resonant beams, we have introduced the TIM technique and employed matrix representation to characterize and describe the TIM. From Fig. 5, lenses L1, L2 with focal length f_1 , f_2 compose the TIM, which can be depicted as:

$$\begin{aligned} \mathbf{M}_{\text{TIM}} &= \mathbf{M}_{L_2} \mathbf{M}_I \mathbf{M}_{L_1} \\ &= \begin{bmatrix} 1 & 0 \\ -\frac{1}{f_2} & 1 \end{bmatrix} \begin{bmatrix} 1 & l_t \\ 0 & 1 \end{bmatrix} \begin{bmatrix} 1 & 0 \\ -\frac{1}{f_1} & 1 \end{bmatrix} \\ &= \begin{bmatrix} \frac{1}{M} & l_t \\ 0 & M \end{bmatrix}, \end{aligned} \quad (12)$$

where $M = -f_1/f_2$.

Building on the previously mentioned matrices and referring to Fig. 5, we can define the one trip beams transmission in the resonator. Taking reflector M1 as the starting point, the beam propagating in the cavity will pass through lens 1, lens 2, and reflector M2 in sequence. This process can be expressed using the following matrix representation:

$$\begin{aligned} \mathbf{M}_c &= \mathbf{M}_{M_2} \mathbf{M}_{d_3} \mathbf{M}_{L_2} \mathbf{M}_I \mathbf{M}_{L_1} \mathbf{M}_{d_2} \mathbf{M}_{d_1} \mathbf{M}_{M_1} \\ &= \begin{bmatrix} -1 & 0 \\ \frac{1}{f_{r2}} & -1 \end{bmatrix} \begin{bmatrix} 1 & d_3 \\ 0 & 1 \end{bmatrix} \begin{bmatrix} 1 & 0 \\ -\frac{1}{f_2} & 1 \end{bmatrix} \begin{bmatrix} 1 & l_t \\ 0 & 1 \end{bmatrix} \\ &\quad \begin{bmatrix} 1 & 0 \\ -\frac{1}{f_1} & 1 \end{bmatrix} \begin{bmatrix} 1 & d_2 \\ 0 & 1 \end{bmatrix} \begin{bmatrix} 1 & d_1 \\ 0 & 1 \end{bmatrix} \begin{bmatrix} -1 & 0 \\ \frac{1}{f_{r1}} & -1 \end{bmatrix}, \end{aligned} \quad (13)$$

where \mathbf{M}_{M_1} , \mathbf{M}_{M_2} , \mathbf{M}_{L_1} , and \mathbf{M}_{L_2} express the matrix of reflector M1, M2 with effective curvature factors ρ_1 and f_{r2} , and lenses L1, L2 with focal length f_1 and f_2 . \mathbf{M}_{d_1} , \mathbf{M}_{d_2} , \mathbf{M}_{d_3} , and \mathbf{M}_I express the beam transfer in the space with distances d_1 , d_2 , d_3 and l_t .

To accurately determine the diffraction loss, it is essential to depict the beam's distribution along the vertical propagation direction. The beam spot effectively characterizes the beam's vertical distribution, with its radius being a commonly used metric to evaluate the beam's lateral amplitude at a given

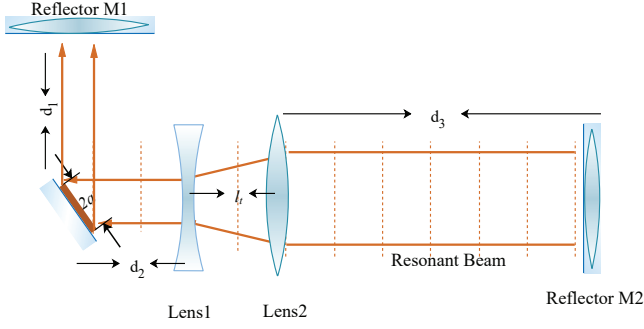


Fig. 5. Resonator structure (d_1, d_2, d_3, l_t : elements distance; a : radius of gain medium)

point. Given that the intensity cross-section of the beam is circular, we utilize the spot radius as the key parameter for this evaluation. According to [30], [31], the beam spots radius on the reflectors of the resonant cavity can be defined by M_c . Furthermore, given that the gain medium is strategically positioned on the transmitter side, and considering that the distance d_1 is relatively small, it can be inferred that the spot size on the gain medium is approximately equivalent to the spot size on reflector M1. In this case, the beam spot radius on the gain medium can be given by:

$$\begin{cases} M_c = \begin{bmatrix} A_c & B_c \\ C_c & D_c \end{bmatrix} \\ \omega_g = \left(-\frac{\lambda^2 B_c D_c}{\pi^2 A_c C_c} \right)^{1/4}, \end{cases} \quad (14)$$

where A_c , B_c , C_c , and D_c are the matrix elements of M_c which is depicted in (13); λ is the wavelength of the resonant beam. Further, the beam diffraction loss V_d can be defined as [32]:

$$V_d = 1 - \exp(-2a^2/w_g^2), \quad (15)$$

where a denotes the radius of gain medium.

D. Electric Power output and Spectral Efficiency

As outlined in Section II.A, the external beam carrying the signal will emerge from reflector M2 at the receiver's end. Subsequently, a beam splitter is employed to divide this external beam into two distinct paths. One portion is directed towards the photovoltaic (PV) cell, facilitating electric energy harvesting (EH). The other portion is captured by the Avalanche Photodiode (APD) for the purpose of data reception.

1) *Electric power output*: Firstly, part of the external beam separated by the beam splitter is transmitted to the surface of the photovoltaic cell through a homogenizing waveguide. Then, the beam will be converted into electrical power output through photoelectric conversion. This process can be briefly expressed by the following formula [33]:

$$\begin{cases} P_p = \mu P_{\text{beam}}, \\ P_{\text{Eout}} = \eta_p P_p + P_{\text{pth}}, \end{cases} \quad (16)$$

where μ is the power split ratio, P_p expresses the beam power received by the PV. The parameter η_p is the slope efficiency of photoelectric conversion, and P_{pth} is the threshold power of PV. It should be noted that, in order to simplify the simulation process, P_{Eout} is represented using a linear model. This approach is based on the experimental findings presented in [34], and assumes ideal conditions for both heat dissipation and the receiving area of the PV (photovoltaic) system. In practice, the beam energy absorbed by PV is limited, it is expected that the conventional linear EH model is only accurate for the specific scenario when the received powers at the receiver is in a constant power range and the nonlinear EH model has a better applicability [35]. Further, the end-to-end energy conversion efficiency is depicted as:

$$\eta_E = \frac{\eta_p P_p + P_{\text{pth}}}{P_{\text{in}}}. \quad (17)$$

2) *Spectral efficiency*: The residual portion of the external beam, segregated by the beam splitter, is incident upon the APD. The APD functions to convert this optical signal into an electrical signal, concurrently facilitating data reception. This conversion process can be illustrated as follows:

$$\begin{cases} P_D = (1 - \mu) P_{\text{beam}}, \\ I_{\text{Dout}} = \nu P_D, \end{cases} \quad (18)$$

where ν is the optical-to-electrical conversion responsivity of APD.

Moreover, photoelectric conversion will produce thermal noise and shot noise when APD is receiving data. Among them, thermal noise can be expressed by the following formula [36]:

$$n_{\text{thermal}}^2 = \frac{4kTB_x}{R_L}, \quad (19)$$

where k is the Boltzmann constant, T is the background temperature, and R_L is the load resistor. In addition, the formula about the shot noise factor is [36]

$$n_{\text{shot}}^2 = 2q(I_{\text{Dout}} + I_{\text{bg}})B_x, \quad (20)$$

where q is the electron charge, B_x is the bandwidth, I_{bg} is the background current. At this point, the additive white Gaussian noise (AWGN) of the communication module can be defined:

$$N_M^2 = n_{\text{shot}}^2 + n_{\text{thermal}}^2. \quad (21)$$

Finally, we can obtain spectral efficiency of the system as [37]:

$$\tilde{C} = \frac{1}{2} \log_2 \left(1 + \frac{I_{\text{Dout}}^2}{2\pi e N_M^2} \right), \quad (22)$$

where e is the natural constant.

III. SIMULATION CALCULATIONS AND RESULTS ANALYSIS

In this section, we will evaluate the performance of the proposed system by analyzing the resonant beam distribution, received beam power, output electric power and channel capacity.

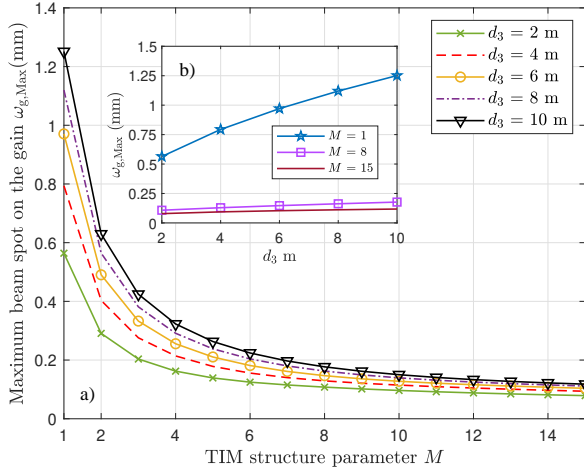


Fig. 6. a) Maximum beam radius on the gain versus TIM structure parameter for different curvature of reflector M2; b) Maximum beam radius on the gain versus end-to-end distance

A. Resonant Beam Distribution

In order to match the semiconductor gain, the proposed RB system introduce a built-in TIM, which can modulate the phase of the beam to achieve the beam compression. To evaluate the compression performance, we apply the beam spot radius defined in the previous chapter, analyzing its changes with different structure parameters.

1) *Parameter Setting*: The gain medium is composed of semiconductor material GaAsP, which can generate light beam with 980 nm wavelength. It is placed obliquely and is 20 mm away from M1. Based on the Section II.C, we take the value of f_{r1} as infinite ($d = f$). Then, to constrain the beam to maintain par-axial propagation, the f_{r2} of M2 is set as variable. The TIM is positioned on the side of the gain medium, and its position parameter is set to $d_2 = 20$ mm relative to the gain chip. The focal length of the concave lens of the TIM is designed as $f_1 = -5$ mm. We take the end-to-end distances d_3 from 2 m to 10 m, and TIM structure parameter M as the inspection point, respectively. Finally, considering the beam spot radius will be different at different distances, we take the maximum value of the spot radius $\omega_{g,Max}$ on the gain medium to evaluate.

2) *Calculation results and analysis*: Fig. 6(a) presents the calculation results which depicts the relationship of the TIM structure parameter M and the maximum beam spot radius $\omega_{g,Max}$. As can be seen, when the value of M increases, the $\omega_{g,Max}$ shows a downward trend. When M is in the range of 2 to 6, the beam radius decreases rapidly. Then, when M is greater than 10, the decline of the beam spot tends to be gentle, which indicates that compression capacity is limited. Moreover, if the M is beyond the range, the compression tends to be stable, and if d_3 takes a large value, the overall $\omega_{g,Max}$ will increase. In numerical, the incident beam can be compressed from 1.2 mm to around 0.1 mm, which is only 1/12 of the original beam. Fig. 6(b) depicts curves of $\omega_{g,Max}$ as a function of d_3 . As it presented, in the original scheme without TIM (where M equals 1), the radius of beam presents

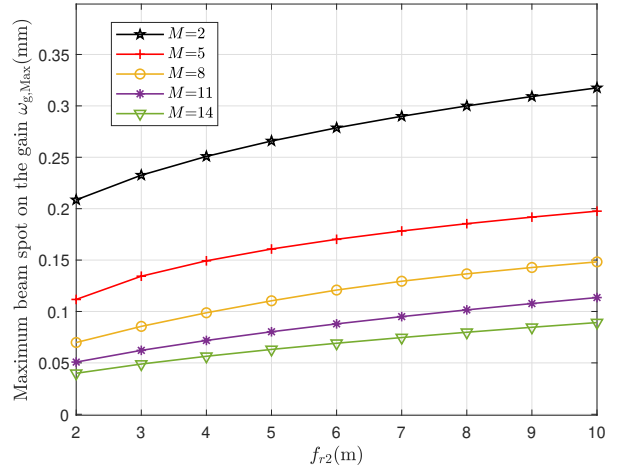


Fig. 7. Maximum beam radius on the gain versus f_r parameters of reflector M2 with different TIM structure parameter

a great trend of increase when d_3 enhances. In contrast, the proposed scheme with TIM shows a gentle trend of increase. Numerically, the value of $\omega_{g,Max}$ in proposed scheme is below 0.25 mm while the original scheme is great then 0.5 mm. Further, we analyze the influence of f_r parameter on beam compression. Fig. 7 describes curves of maximum beam radius on the gain versus f_r parameters of reflector M2. As depicted, $\omega_{g,Max}$ exhibits an upward trend as the value of f_{r2} increases. Subsequently, the curves demonstrate a downward shift with the increase in the value of M . Overall, the increase in f_{r2} tends to have a detrimental effect on beam compression, as evidenced by the enlargement of the beam spot.

From the aforementioned analysis, preliminary conclusions can be obtained that the TIM can effectively compress the beam under different end-to-end distance. Based on Section II.A&B, this ability ensures that the resonant beam can enter the micron-level size semiconductor gain without causing large energy loss.

B. Received Beam Power

According to Section II.A, after the energy accumulating, the external beam will eventually emerge from reflector M2. Then, it will enter the PV and APD respectively under the function of the beam splitter, realizing the electric power output and data reception. Usually, we can adopt the received beam power P_{beam} to evaluate the end-to-end beam transmission performance.

1) *Parameter Setting*: The gain medium is made of GaAsP. According to the material properties, we set the characteristic parameters such as light quantum, gain factor, etc. and list them in Table I. Furthermore, we adopt a typical laser diode as the pump source whose electro-optical conversion efficiency η_{pc} and absorption efficiency η_{pa} are 0.6 and 0.85. In addition, the effective active cross-section A_s of the gain is set as 3×10^{-4} cm², the constant loss V_c takes 0.99, the geometric radius of gain medium a is 0.5 mm, the pump beam wavelength is 808 nm, the reflectivity of the mirror in M1 is 0.999, and the end-to-end transmission distance is 10 m.

TABLE I
PARAMETERS OF THE GAIN MEDIUM [29]

Parameter	Symbol	Value
Gain factor	g_0	2000 cm^{-1}
Transparency carrier density	N_0	$1.7 \times 10^{18} \text{ cm}^{-3}$
Longitudinal confinement factor	Γ	2.0
Light speed	c	$3 \times 10^8 \text{ m/s}$
Planck constant	h	$6.6260693 \times 10^{-34} \text{ J}$
Monomolecular recombination coefficient	α	10^7 sec^{-1}
Bimolecular recombination coefficient	β	$10^{-10} \text{ cm}^3/\text{sec}$
Auger recombination coefficient	γ	$6 \times 10^{-30} \text{ cm}^6/\text{sec}$

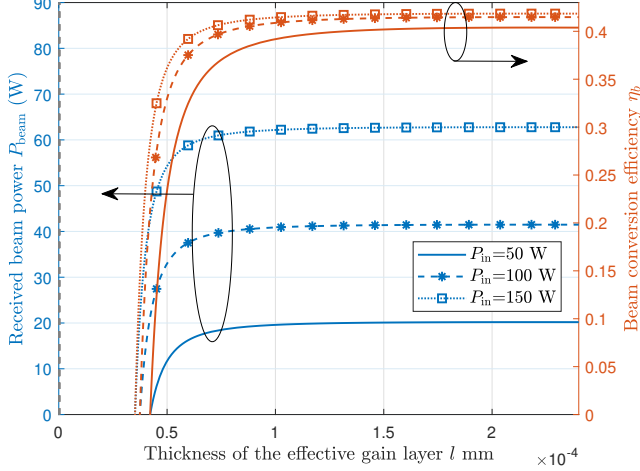


Fig. 8. Received beam power and conversion efficiency versus thickness of the effective gain layer

2) *Calculation results and analysis*: Fig. 8 describes the relationship among the received beam power (P_{beam}), conversion efficiency (η_b), and the thickness of the effective gain layer (l). It is observed that as l increases, both P_{beam} and η_b exhibit a rising trend. However, this upward trend tends to plateau when the thickness of the effective gain layer reaches a larger value. Consequently, the influence of l on both P_{beam} and η_b becomes less pronounced. Moreover, when P_{in} takes a large value, curves of P_{beam} and η_b will move up. In numerical, the received beam power can be 60 W and beam conversion efficiency can be 40 % as $P_{\text{in}}=150$ W, and the increase of P_{in} has great impact on P_{beam} while has insignificant impact on η_b . Overall, by **appropriately** increasing the thickness, we can **enhance** the performance of beam transmission.

Fig. 9 presents the curves of received beam power and conversion efficiency versus reflectivity of M2. From the blue lines in the graph, it is evident that as the reflectivity of mirror M2 (R_2) changes from 0.8 to 1, both the received beam power and the beam conversion efficiency initially increase and then decrease. Moreover, as the input power is increased, the curves representing the beam power (P_{beam}) and the beam conversion efficiency (η_b) shift to the left and ascend. Numerically, the maximum value of P_{beam} and η_b are obtained when the R_2 locates at the range from 0.9 to 0.95.

In Fig. 10, we analyze P_{beam} and η_b as the function of the input power P_{in} . According to the blue lines, the P_{beam} will increase as P_{in} increase, which presents a positive linear

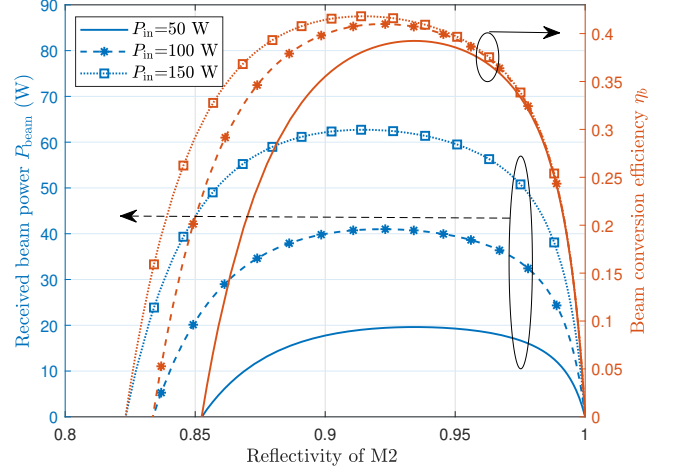


Fig. 9. Received beam power and conversion efficiency versus reflectivity of M2

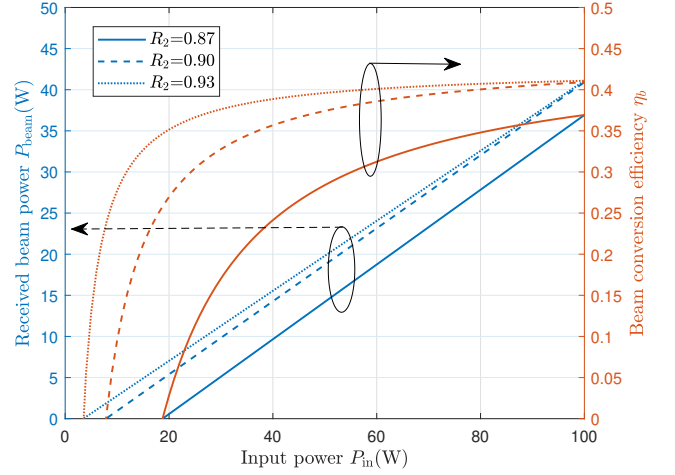


Fig. 10. Received beam power and conversion efficiency versus input power

relationship with P_{in} . Moreover, the slope and intercept of lines are affected by R_2 . A large value of R_2 is benefit for reducing the threshold power (line intercept). Besides, from the red curves, the η_b will be also enhanced by P_{in} increase. However, different from P_{beam} , curves are nonlinear and gradually flattens out. **Further, we evaluate the performance of received beam power P_{beam} as the function of transmission distance d_3 , which is shown in Fig. 11. As can be seen, curves of P_{beam} present a downtrend with the increase of the d_3 which proves the negative impact of the transmission loss on beam output (Section II.C). What's more, with the value of M increases, curves become flattened. It indicted that the transmission loss can be restrained by TIM. In numerical, the value of P_{beam} can maintain 40W output over 15m distance.**

C. Output Electric Power and Channel Capacity

To evaluate the received beam power, we have examined the factors influencing both P_{beam} and η_b . Additionally, it is necessary to analyze the performance of the PV cell and the

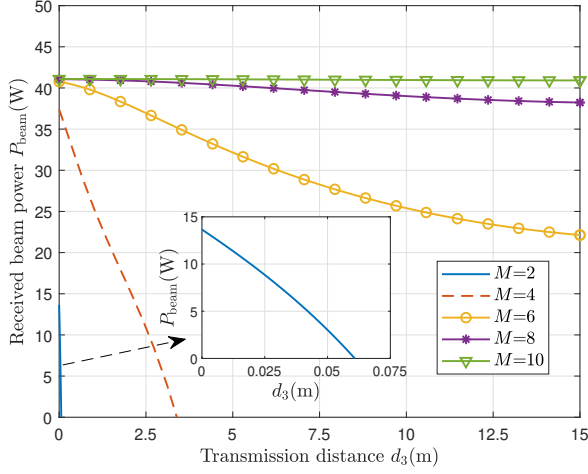


Fig. 11. Received beam power versus transmission distance

APD in the context of simultaneous wireless information and power transfer (SWIPT).

1) *Parameter Setting*: To evaluate the SWIPT performance, the PV and APD structure parameters should be defined. According to [34], PV cell structure parameters η_p and P_{pth} are set as 0.3487 and -1.535 W, respectively. In the proposed system, the environment temperature is taken as $T=300$ K, the electronic charge q is 1.6×10^{-19} C, and the Boltzmann constant k is 1.38×10^{-23} J/K. The APD for light signal receiving is commercial sensors for 980 nm wavelength. Then, based on [36], [38]–[40], we set the conversion responsivity of the APD $\nu=0.6$ A/W, the noise bandwidth $B_x=811.7$ MHz, the background current $I_{bg}=5100$ μ A, and the load resistance $R_L=10$ K Ω .

2) *Calculation results and analysis*: Fig 12 depicts the curves of spectral efficiency, output electric power, and end-to-end conversion efficiency versus beam splitting ratio. Observing the blue line, the entire curve exhibits a downward trend as μ increases. Initially, this decline is relatively gradual. However, when μ exceeds 0.8, \tilde{C} starts to decrease sharply. From the red and green lines with markers, it is evident that both P_{Eout} and η_E exhibit a positive linear relationship with μ . Their values increase as μ increases. Numerically, the spectral efficiency \tilde{C} can reach 17.69 bit/s/Hz when μ is set to 0.99, at which point P_{Eout} and η_E are also high. Therefore, this value of μ can be chosen as the beam splitting ratio to achieve high-efficiency SWIPT.

Besides, we also explore the relationship of spectral efficiency, output electric power, and end-to-end conversion efficiency versus input power, which is presented in Fig. 13. From the blue line, it's apparent that the spectral efficiency rapidly ascends to a larger value. In general, the greater the input beam energy, the higher the spectral efficiency the scheme achieves. However, this effect is somewhat limited. As the input power continues to increase, the system's spectral efficiency tends to stabilize. For instance, when P_{in} is increased from 50W to 150W, the spectral efficiency experiences only a modest increase of 1 bit/s/Hz. Furthermore, as indicated by

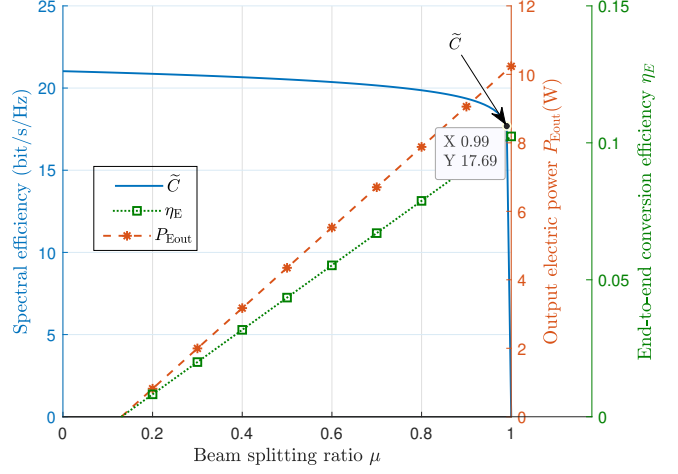


Fig. 12. Spectral efficiency, output electric power, and end-to-end conversion efficiency versus beam split ratio ($P_{in}=100$ W)

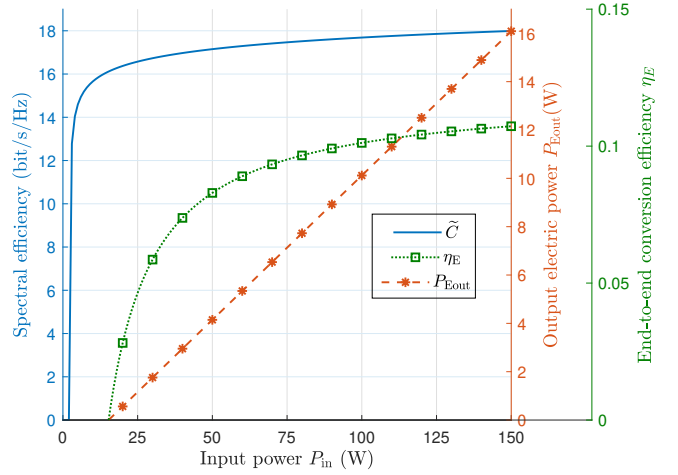


Fig. 13. Spectral efficiency, output electric power, and end-to-end conversion efficiency versus input power ($\mu=0.99$)

the red and green lines, both P_{Eout} and η_E exhibit a positive relationship with P_{in} , where P_{Eout} shows a linear trend and η_E demonstrates a nonlinear one. In numerical, P_{Eout} and η_E can reach up to 16 W and 0.11, respectively, at $P_{in} = 150$ W. Generally, by optimally matching the splitting ratio with the input power, the system's data transmission spectral efficiency can achieve 16-18 bit/s/Hz, supporting 0-16 W of electric power. This demonstrates the system's potential for high-rate and high-power SWIPT.

D. Summary

In summary, after numerical evaluation and analysis, we conclude that the proposed RB SWIPT scheme is capable of providing 16 W electrical energy harvesting and 18 bit/s/Hz spectral efficiency for communication, with 11% energy conversion efficiency and 10 m transmission distance. Table II presents the performance comparison between our system and the existing architectures, clearly demonstrating the advantages

TABLE II
COMPARISON OF EXISTING SWIPT SCHEMES

Technology	Ref.	Conversion Efficiency	Spectral Efficiency	Output Power	Transmission Distance
Visible light	[41]	$0.38 \times 10^{-4}\%$	6 bit/s/Hz	2.96 mW	1.5 m
	[42]	$8.44 \times 10^{-5}\%$	8 bit/s/Hz	0.38 mW	3.0 m
Radio frequency	[43]	$1.375 \times 10^{-4}\%$	Not stated	$5.5 \mu\text{W}$	15 m
	[44]	$5 \times 10^{-2}\%$	7 bit/s/Hz	5 mW	10 m
Resonant beam	[13]	1%	Not stated	2W	2.6 m
	This work	11%	18 bit/s/Hz	16W	15 m

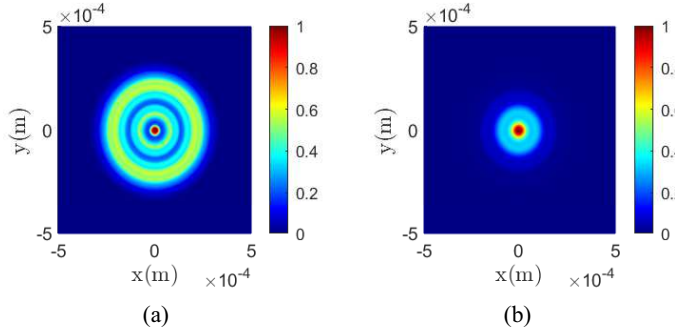


Fig. 14. Field distribution on the gain medium: (a)without TIM; (b)with TIM

of the proposed RB SWIPT in delivering high power, maintaining high spectrum efficiency, and ensuring high energy conversion efficiency over long transmission distances.

IV. DISCUSSION

A. Transmission Model by Electromagnetic Field Propagation

In the aforementioned sections, we have developed end-to-end beam transmission model based on linear optics using beam matrices. Additionally, considering the electromagnetic field characteristics of light waves, we can also adopt electromagnetic field propagation to conduct exact analyses for the amplitude and phase distribution of the light field. The theoretical framework for describing electromagnetic field propagation is derived from Maxwell's equations, leading to the wave equations for electric and magnetic fields, as cited in [45]. Furthermore, according to Huygens-Fresnel principle, during the propagation of light, the field distribution at any point is determined by the coherent superposition of the wavelets of the incident wave at that point [46]. By understanding the field distribution of the initial point light wave, denoted as $u(x, y)$, we can apply diffraction theory to express its field distribution at a specific point 's' on the transmission path as $u'(x, y)$. This approach allows us to accurately represent the beam transmission within the resonator. Building on this, we can incorporate the boundary conditions of the resonator in our proposed system to describe the changes in the light field of the beam over a complete end-to-end cycle. Furthermore, by considering the beam generation from the self-reproductive mode, as mentioned in [47], as a criterion for stable output, we can determine the steady-state light field distribution.

Fig. 14 presents the field distribution on the gain medium based on the electromagnetic field propagation model. As can

be seen, the incident beam on the gain medium has been effectively compressed in the proposed system with TIM. In contrast, beam has a large field distribution with low beam quality (uneven distribution) in the original system without TIM. This analysis corresponds to the results obtained using the matrix model in Section V, further verifying the feasibility of our proposed scheme. Overall, electromagnetic field propagation analysis is beneficial for evaluating the beam's quality, system structure, etc. However, it's important to note that as fast Fourier transform and the Fox-Li iterative method are employed in these calculations, they demand significantly more computing power and time compared to the transmission matrix method introduced in the second section of this paper. Future research will delve deeper into the benefits and results of this method.

B. System Experiment and Applications

In this paper, we propose a high-efficiency RB charging and communication scheme, provide an analytical model, and evaluate system performance through simulation. For practical implementation of the RB-SWIPT scheme in IoT applications, we should discuss the system deployment and applications in IoT.

1) System deployment: As illustrated in Fig.2 and Fig.5, the system incorporates several lenses. These lenses can be made of N-BK7 glass, known for its high laser damage threshold, and are coated with an anti-reflective layer to reduce beam loss. Reflectors M1 and M2 are designed with a cat-eye structure, as detailed in Section II.C. This design includes a convex lens and a flat mirror aligned in parallel, with their optical centers overlapping to create a focus-free system. Additionally, reflectors utilizing a corner-cube structure, as shown in Fig. 15.(a), are also suitable for this system to facilitate beam retro-reflection. Furthermore, to realize beam separated, optical splitters are introduced in the receiver. Normally, beam splitters such as cube beam-splitters can be used to separate the external beam, which are demonstrated in Fig. 15(b). Cube beam-splitter consists of two classical right angle prisms which can also consist by N-BK7 glasses. The hypotenuse surface of one prism has a coating for beam splitting, and the two prisms are cemented together, forming a cubic shape. When beams incident, part of the beam will transmit through it, and the other part of the beam is reflected by the coating and propagates in the vertical incident direction.

The gain module utilized in our system is an open-cavity surface-emitting semiconductor gain, requiring specific customization. As depicted in Fig. 3, the semiconductor gain

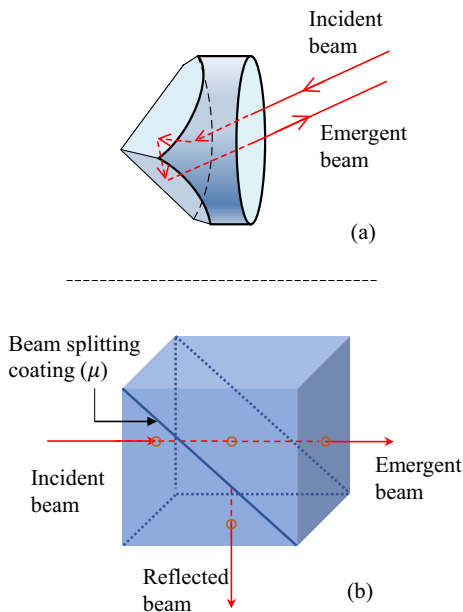


Fig. 15. (a) Corner-cube reflector; (b) Cube beam-splitter

module is composed of several material regions. Central to these is the Distributed Bragg Reflector (DBR) layer and the gain layer, both of which are fabricated using material growth equipment. This fabrication process involves creating a multi-layer stack structure with alternating high and low refractive indices, along with the quantum well structure previously mentioned. The topmost layer of the module serves as the photon exit for light emission, which can be optimized with an anti-reflection coating to minimize optical losses. The bottom layer functions as a thermal dissipation layer, typically made from a high thermal conductivity metal that is compatible with the semiconductor materials used. Drawing on the analysis of the critical experimental factors previously discussed, and through the rational arrangement of components, we can effectively construct the experimental platform.

2) System applications: To demonstrate the practical applications of our system, consider its use in real-time Internet of Things (IoT) scenarios, such as with unmanned aerial vehicles (UAVs). UAVs, known for their exceptional mobility, are excellent candidates for acting as aerial nodes. This role not only extends network coverage but also enhances the flexibility of IoT topology. However, employing UAVs in this capacity requires the system to have robust endurance and superior communication capabilities. The RB-SWIPT system is ideally suited for this purpose, as it can effectively power UAVs while ensuring reliable data transmission. We introduce a composite UAV system design, comprising a short-endurance UAV, an RB-SWIPT station, and a set of buoy sensors. The UAV's fuselage is equipped with the RB-SWIPT station's receiver module, enabling wireless charging through resonant beam. This feature is crucial when the UAV is tasked with collecting data from sensors, adjusting its flight path, or functioning as a 'thing' node in the IoT network. The use of resonant beam technology not only facilitates reliable data transmission

but also helps maintain a higher state of charge for the UAVs. However, the original resonant optical system faced limitations in transmission distance and conversion efficiency due to energy losses, with a maximum transmission distance of only 2.6 meters and a mere 1% conversion efficiency, as reported in [13]. These limitations hindered its application in UAVs. Thus, the innovative approach presented in this paper, which integrates a TIM structure and high-efficiency semiconductor gain modules, significantly enhances both the transmission distance and conversion efficiency. This improvement makes the application of the resonant beam system in UAVs feasible. Furthermore, we have developed a viable communication pathway that facilitates simultaneous energy transmission and information delivery. The establishment of a reliable optical communication channel addresses bandwidth and interference challenges, effectively integrating UAVs as functional nodes in IoT applications. Beyond the UAV application mentioned above, the RB-SWIPT system is versatile enough to be integrated with a wide range of real-time IoT terminals. Examples include human body sensors, cameras, smart doorbells, and other IoT devices. The implementation of this system can effectively address common challenges such as the need for extensive device wiring, excessive battery usage, and radio signal interference. This is achieved by enabling real-time energy and signal transmission, thereby enhancing the efficiency and reliability of IoT networks.

V. CONCLUSIONS

In this paper, we have introduced a high-efficiency resonant beam charging and communication system, which utilizes a semiconductor gain medium and a telescope internal modulator. Grounded in the theories of beam transmission, power conversion, energy harvesting, and data reception, we developed comprehensive analytical models. These models address the beam propagation, beam power, electric power output, and spectral efficiency of our proposed system. Numerical analyses demonstrate that our system exhibits exceptional Simultaneous Wireless Information and Power Transfer (SWIPT) performance. It is capable of producing 16 W of electric power output with an 11% end-to-end conversion efficiency and supporting a spectral efficiency of 18 bit/s/Hz for communication purposes.

There are compelling topics that warrant further investigation in future studies. 1) With respect to the performance of the proposed scheme during actual deployment, its influencing factors, and the discrepancies with the simulation results, the experimental analysis of the system can be conducted in the future. 2) The integration of the proposed system scheme into existing IoT devices, such as system integration, energy reception circuit design, and communication module design, should be thoroughly researched in the future.

REFERENCES

- [1] M. Series, "IMT vision—framework and overall objectives of the future development of IMT for 2020 and beyond," *Recommendation ITU*, vol. 2083, 2015.
- [2] K. Jin and W. Zhou, "Wireless laser power transmission: a review of recent progress," *IEEE transactions on power electronics*, vol. 34, no. 4, pp. 3842–3859, Jul. 2018.

- [3] S. Y. R. Hui, W. Zhong, and C. K. Lee, "A critical review of recent progress in mid-range wireless power transfer," *IEEE Transactions on Power Electronics*, vol. 29, no. 9, pp. 4500–4511, Mar. 2013.
- [4] X. Lu, P. Wang, D. Niyato, D. I. Kim, and Z. Han, "Wireless charging technologies: Fundamentals, standards, and network applications," *IEEE Communications Surveys & Tutorials*, vol. 18, no. 2, pp. 1413–1452, Nov. 2015.
- [5] J. Lim, T. S. Khwaja, and J. Ha, "Wireless optical power transfer system by spatial wavelength division and distributed laser cavity resonance," *Opt. Express*, vol. 27, no. 12, pp. A924–A935, Jun 2019.
- [6] Y. Huang and B. Clerckx, "Waveform design for wireless power transfer with limited feedback," *IEEE Transactions on Wireless Communications*, vol. 17, no. 1, pp. 415–429, Nov. 2017.
- [7] B. Scrosati and J. Garce, "Lithium batteries: Status, prospects and future," *Journal of power sources*, vol. 195, no. 9, pp. 2419–2430, May. 2010.
- [8] R. W. Habash, J. M. Elwood, D. Krewski, W. G. Lotz, J. P. McNamee, and F. S. Prato, "Recent advances in research on radiofrequency fields and health: 2004–2007," *Journal of Toxicology and Environmental Health, Part B*, vol. 12, no. 4, pp. 250–288, Aug. 2009.
- [9] H. Elgala, R. Mesleh, and H. Haas, "Indoor optical wireless communication: potential and state-of-the-art," *IEEE Communications Magazine*, vol. 49, no. 9, pp. 56–62, Sept. 2011.
- [10] H. Li and Y. Huang, "The architecture of blind equalizer for mimo free space optical communication system," in *Optical Communication, Optical Fiber Sensors, and Optical Memories for Big Data Storage*, vol. 10158. International Society for Optics and Photonics, Oct. 2016, p. 101581H.
- [11] A. Ortal, Z. Nes, P. Rudiger, and Zurich, "Wireless laser system for power transmission utilizing a gain medium between retroreflectors," U.S. Patent 9 653 949, May 16, 2017.
- [12] Q. Liu, J. Wu, P. Xia, S. Zhao, W. Chen, Y. Yang, and L. Hanzo, "Charging unplugged: Will distributed laser charging for mobile wireless power transfer work?" *IEEE Vehicular Technology Magazine*, vol. 11, no. 4, pp. 36–45, Dec. 2016.
- [13] W. Wang, Q. Zhang, H. Lin, M. Liu, X. Liang, and Q. Liu, "Wireless energy transmission channel modeling in resonant beam charging for IoT devices," *IEEE Internet of Things Journal*, vol. 6, no. 2, pp. 3976–3986, Apr. 2019.
- [14] M. Liu, H. Deng, Q. Liu, J. Zhou, M. Xiong, L. Yang, and G. B. Giannakis, "Simultaneous mobile information and power transfer by resonant beam," *IEEE Transactions on Signal Processing*, pp. 1–1, May. 2021.
- [15] W. Fang, H. Deng, Q. Liu, M. Liu, Q. Jiang, L. Yang, and G. B. Giannakis, "Safety analysis of long-range and high-power wireless power transfer using resonant beam," *IEEE Transactions on Signal Processing*, May. 2021.
- [16] M. A. Khalighi and M. Uysal, "Survey on free space optical communication: A communication theory perspective," *IEEE communications surveys & tutorials*, vol. 16, no. 4, pp. 2231–2258, Jun. 2014.
- [17] W. Chen, S. Zhao, Q. Shi, and R. Zhang, "Resonant beam charging-powered UAV-assisted sensing data collection," *IEEE Transactions on Vehicular Technology*, vol. 69, no. 1, pp. 1086–1090, Oct. 2019.
- [18] X. Liu, Y. Liu, Y. Chen, and L. Hanzo, "Trajectory design and power control for multi-UAV assisted wireless networks: A machine learning approach," *IEEE Transactions on Vehicular Technology*, vol. 68, no. 8, pp. 7957–7969, May. 2019.
- [19] Q. Sheng, M. Wang, H. Ma, Y. Qi, J. Liu, D. Xu, W. Shi, and J. Yao, "Continuous-wave long-distributed-cavity laser using cat-eye retroreflectors," *Opt. Express*, vol. 29, no. 21, pp. 34 269–34 277, Oct. 2021.
- [20] Z. Zhang, J. Zhang, Y. Zhou, X. Zhang, Z. Li, J. Zhang, J. Zhang, Y. Gong, T. Liu, J. Mu *et al.*, "2m-distance external cavity vcsel for wireless charging applications," *Optics Express*, vol. 30, no. 13, pp. 22 364–22 375, Jun. 2022.
- [21] M. Xiong, M. Liu, Q. Zhang, Q. Liu, J. Wu, and P. Xia, "TDMA in adaptive resonant beam charging for IoT devices," *IEEE Internet of Things Journal*, vol. 6, no. 1, pp. 867–877, Feb. 2018.
- [22] M. Xiong, Q. Liu, M. Liu, X. Wang, and H. Deng, "Resonant beam communications with photovoltaic receiver for optical data and power transfer," *IEEE Transactions on Communications*, vol. 68, no. 5, pp. 3033–3041, Feb. 2020.
- [23] M. S. Aziz, S. Ahmad, I. Husnain, A. Hassan, and U. Saleem, "Simulation and experimental investigation of the characteristics of a pv-harvester under different conditions," in *2014 International Conference on Energy Systems and Policies (ICESP)*. IEEE, Nov. 2014, pp. 1–8.
- [24] J. C. Campbell, "Recent advances in telecommunications avalanche photodiodes," *Journal of Lightwave Technology*, vol. 25, no. 1, pp. 109–121, Jan 2007.
- [25] W. W. Chow, S. W. Koch, and M. I. Sargent, *Semiconductor-laser physics*. Springer Science & Business Media, 2012.
- [26] H. Soda, K. ichi Iga, C. Kitahara, and Y. Suematsu, "GaInAsP/InP surface emitting injection lasers," *Japanese Journal of Applied Physics*, vol. 18, no. 12, pp. 2329–2330, dec 1979.
- [27] H. Soda, Y. Motegi, and K. Iga, "GaInAsP/InP surface emitting injection lasers with short cavity length," *IEEE Journal of Quantum Electronics*, vol. 19, no. 6, pp. 1035–1041, Jun. 1983.
- [28] W. Koechner, *Solid-state laser engineering*. Springer, 2013, vol. 1.
- [29] M. Kuznetsov, F. Hakimi, R. Sprague, and A. Mooradian, "Design and characteristics of high-power (0.5-W CW) diode-pumped vertical-external-cavity surface-emitting semiconductor lasers with circular TEM₀₀ beams," *IEEE Journal of Selected Topics in Quantum Electronics*, vol. 5, no. 3, pp. 561–573, May. 1999.
- [30] P. Baues, "Huygens' principle in inhomogeneous, isotropic media and a general integral equation applicable to optical resonators," *Optoelectronics*, vol. 1, no. 1, pp. 37–44, Feb. 1969.
- [31] V. Magni, "Multielement stable resonators containing a variable lens," *JOSA A*, vol. 4, no. 10, pp. 1962–1969, Oct 1987.
- [32] S. Cao, S. Tu, Y. Huang, H. Fan, J. Li, H. Xia, and G. Ren, "Analysis of diffraction loss in laser resonator," *Laser Technol.*, vol. 42, no. 3, pp. 400–403, May. 2018.
- [33] Q. Zhang, W. Fang, M. Xiong, Q. Liu, J. Wu, and P. Xia, "Adaptive resonant beam charging for intelligent wireless power transfer," *IEEE Internet of Things Journal*, vol. 6, no. 1, pp. 1160–1172, Feb. 2018.
- [34] Q. Zhang, W. Fang, Q. Liu, J. Wu, P. Xia, and L. Yang, "Distributed laser charging: A wireless power transfer approach," *IEEE Internet of Things Journal*, vol. 5, no. 5, pp. 3853–3864, Oct. 2018.
- [35] E. Boshkovska, D. W. K. Ng, N. Zlatanov, and R. Schober, "Practical non-linear energy harvesting model and resource allocation for swipt systems," *IEEE Communications Letters*, vol. 19, no. 12, pp. 2082–2085, Dec. 2015.
- [36] F. Xu, M. Khalighi, and S. Bourennane, "Impact of different noise sources on the performance of PIN- and APD-based FSO receivers," in *Proceedings of the 11th International Conference on Telecommunications*, Jun. 2011, pp. 211–218.
- [37] A. Lapidot, S. M. Moser, and M. A. Wigger, "On the capacity of free-space optical intensity channels," *IEEE Transactions on Information Theory*, vol. 55, no. 10, pp. 4449–4461, Oct. 2009.
- [38] M. S. Demir, F. Miramirkhani, and M. Uysal, "Handover in VLC networks with coordinated multipoint transmission," in *2017 IEEE International Black Sea Conference on Communications and Networking (BlackSeaCom)*, Jun. 2017, pp. 1–5.
- [39] C. Quintana, Q. Wang, D. Jakonis, X. Piao, G. Erry, D. Platt, Y. Thueux, A. Gomez, G. Faulkner, H. Chun, M. Salter, and D. O'Brien, "High speed electro-absorption modulator for long range retroreflective free space optics," *IEEE Photonics Technology Letters*, vol. 29, no. 9, pp. 707–710, Mar. 2017.
- [40] A. J. Moreira, R. T. Valadas, and A. de Oliveira Duarte, "Optical interference produced by artificial light," *Wireless Networks*, vol. 3, no. 2, pp. 131–140, May. 1997.
- [41] S. Ma, F. Zhang, H. Li, F. Zhou, Y. Wang, and S. Li, "Simultaneous lightwave information and power transfer in visible light communication systems," *IEEE Transactions on Wireless Communications*, vol. 18, no. 12, pp. 5818–5830, Dec. 2019.
- [42] A. M. Abdelhady, O. Amin, B. Shihada, and M.-S. Alouini, "Spectral efficiency and energy harvesting in multi-cell slipt systems," *IEEE Transactions on Wireless Communications*, vol. 19, no. 5, pp. 3304–3318, Feb. 2020.
- [43] X. Lu, P. Wang, D. Niyato, and E. Hossain, "Dynamic spectrum access in cognitive radio networks with rf energy harvesting," *IEEE Wireless Communications*, vol. 21, no. 3, pp. 102–110, Jun. 2014.
- [44] I. Krikidis, S. Timotheou, S. Nikolaou, G. Zheng, D. W. K. Ng, and R. Schober, "Simultaneous wireless information and power transfer in modern communication systems," *IEEE Communications Magazine*, vol. 52, no. 11, pp. 104–110, Nov. 2014.
- [45] R. N. N. Hodgson and I. H. Weber, *Laser Resonators and Beam Propagation*. Springer, 2005, vol. 108.
- [46] T. Teperik, A. Archambault, F. Marquier, and J.-J. Greffet, "Huygens-fresnel principle for surface plasmons," *Optics express*, vol. 17, no. 20, pp. 17 483–17 490, Sept. 2009.
- [47] A. G. Fox and T. Li, "Resonant modes in a maser interferometer," *Bell System Technical Journal*, vol. 40, no. 2, pp. 453–488, Mar. 1961.